REPORT DOCUMENTATION PAGE

Form Approved
OMB No. 074-0188

Public reporting burden for this collection of information is estimated to average 1 hour per response, including the time for reviewing instructions, searching existing data sources, gathering and maintaining the data needed, and completing and reviewing this collection of information. Send comments regarding this burden estimate or any other aspect of this collection of information, including suggestions for reducing this burden to Washington Headquarters Services, Directorate for Information Operations and Reports, 1215 Jefferson Davis Highway, Suite 1204, Arlington, VA 22202-4302, and to the Office of Management and Budget, Paperwork Reduction Project (0704-0188), Washington, DC 20503

1. AGENCY USE ONLY (Leave blank)	2. REPORT DATE	3. REPORT TYPE AND DATES COVERED
	30-09-2009	Final Progress Report Apr 2006-Mar 2009

4. TITLE AND SUBTITLE
MULTISPECTRAL DETECTOR BASED ON AN ARRAY OF CARBON-NANOTUBE QUANTUM WELLS

5. FUNDING NUMBERS
FA9550-06-1-0366

6. AUTHOR(S)
Serhii SHAFRANIUK

7. PERFORMING ORGANIZATION NAME(S) AND ADDRESS(ES)
Northwestern University Dept. of
Physics & Astronomy
2145 N. Sheridan Rd.
Evanston, IL 60208-3112

8. PERFORMING ORGANIZATION REPORT NUMBER

9. SPONSORING / MONITORING AGENCY NAME(S) AND ADDRESS(ES)
Air Force Office of Scientific Research
875 N. Randolf St. Suite 325
AFOSR Arlington, VA 22203-1768

10. SPONSORING / MONITORING AGENCY REPORT NUMBER

11. SUPPLEMENTARY NOTES

12a. DISTRIBUTION / AVAILABILITY STATEMENT
Approved for public release; distribution unlimited

12b. DISTRIBUTION CODE

13. ABSTRACT ***(Maximum 200 Words)***

The research efforts focused on comb arrays of carbon nanotube quantum wells exposed to external weak THz fields. Each of the individual well in the array had been independently controlled by a dc source-drain voltage and covered a narrow spectral sector within the THz domain diapason. The comb array consisted of two different types of carbon nanotube junctions: semiconducting tube junctions and the metallic tube junctions in the Tomonaga-Luttinger liquid (TLL) state. In this way one extends the analyzed spectral diapason from 0.5-7.5 THz covered by the semiconducting comb to 7.5-50 THz covered by the metallic carbon nanotube comb. Besides our approach exploits intrinsic phase-coherent properties of carbon nanotubes which allows improving of the frequency resolution, and reducing of the intrinsic noises considerably.

14. SUBJECT TERMS
THz field nanosensors, carbon nanotube quantum wells, Luttinger liquid, phase coherence, chiral fermions, ac transport, remote detectors, graphene junctions

15. NUMBER OF PAGES
23

16. PRICE CODE

17. SECURITY CLASSIFICATION OF REPORT	18. SECURITY CLASSIFICATION OF THIS PAGE	19. SECURITY CLASSIFICATION OF ABSTRACT	20. LIMITATION OF ABSTRACT
UNCLASSIFIED	UNCLASSIFIED	UNCLASSIFIED	UL

NSN 7540-01-280-5500

Standard Form 298 (Rev. 2-89)
Prescribed by ANSI Std. Z39-18
298-102

Objectives

This research focuses on multispectral analyzing of weak THz signals by carbon nanotube junction arrays. The junction arrays simultaneously determine the electromagnetic field frequency, polarization, and intensity. Our key idea involvoles combining of metallic and semiconducting carbon tubes in the same comb array. We exploit intrinsic phase-coherent properties of carbon nanotubes. This allows improving the analyzer sensitivity up to ~1 fW and reducing the intrinsic and parasitic noises by factor $10\text{-}10^2$. The suggested approach extends the analyzed spectral diapason from 0.5-7.5 THz covered by the semiconducting comb to 7.5-50 THz covered by the metallic tube comb. Practical outcome of this work can be used for stand off detecting of concealed weapon, explosives, toxic substances, and fast moving projectiles.

Practical implementations of multispectral analyzing by carbon nanotube junctions and current experimental studies

Sensors of electromagnetic field are used in many areas of science and technology. These devices analyze the spectrum of electromagnetic waves reflected from various substances. Many chemical analytes, e.g., explosive or toxic materials have pronounced spectral features in the frequency range $\Delta\nu_{\mathbf{EF}} = 0.5 - 50$ THz (see, e.g., Refs. [A-C] and the references there in). Therefore the THz spectral analysis can be effectively used for a stand off identification of those substances. Since the THz waves (T-rays) penetrate through clothing and paper, the security nanosensors are capable of identifying concealed metallic and ceramic objects. Known medical implementations of the T-ray detectors include monitoring the healing of human skin and of body wounds [4]. Most of T-ray detectors available now work in a narrow frequency range, and are bulky and costly.

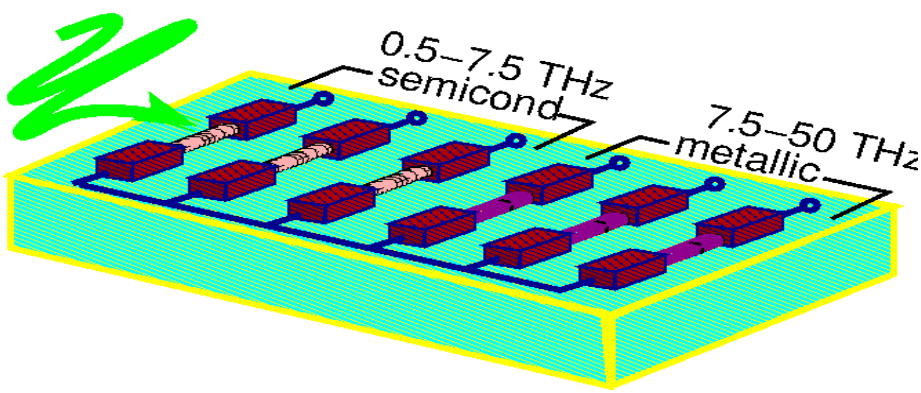

Fig. 1. A comb array of gated carbon nanotube junctions. The setup consists of two parts: the comb of semiconducting nanotubes is used for spectral analyzing of an external electromagnetic field in the diapason 0.5-7.5 Thz while the metallic nanotube comb works in the upper diapason 7.5-50 THz.

This motivates an increased interest to nanoscale devices (nanosensors), which have better sensitivity and wider frequency range. The nanosensors are expected to be more effective, robust, cheaper in mass production, and durable [2,4,5,8,A-D]. The sensing principles exploit a general fact that electron transport in carbon nanotubes is strongly affected by external fields and environment [1-8,A-D]. The central element of the THz multispectral analyzer is a comb array of semiconducting and metallic carbon nanotubes. The comb is placed on a dielectric substrate (in current experiments it is SiO_2). Each of the nanotube in the comb is controlled individually by the bias source drain and gate voltages. The bias voltage control provides an extra flexibility to the spectral analyzer setup since its sensitivity in the whole spectral range is optimized dynamically. The comb array consisted of two different types of carbon nanotube junctions:

semiconducting tube junctions and the metallic tube junctions in the Tomonaga-Luttinger liquid (TLL) state. In this way one extends the analyzed spectral diapason from 0.5-7.5 THz covered by the semiconducting comb to 7.5-50 THz covered by the metallic carbon nanotube comb. Besides our method exploits intrinsic phase-coherent properties of carbon nanotubes which allows improving of the frequency resolution, and reducing of the intrinsic noises considerably.

The relevant experimental work had been conducted at Georgetown University by the Prof. P. Barbara group. Active experimental research of carbon nanotube THz sensors had been conducted also in Japan by Y. Kawano (see Refs. [35-37]). In Fig. 2 we show their recent experimental data which suggest that the carbon nanotube junctions work as sensors of THz field.

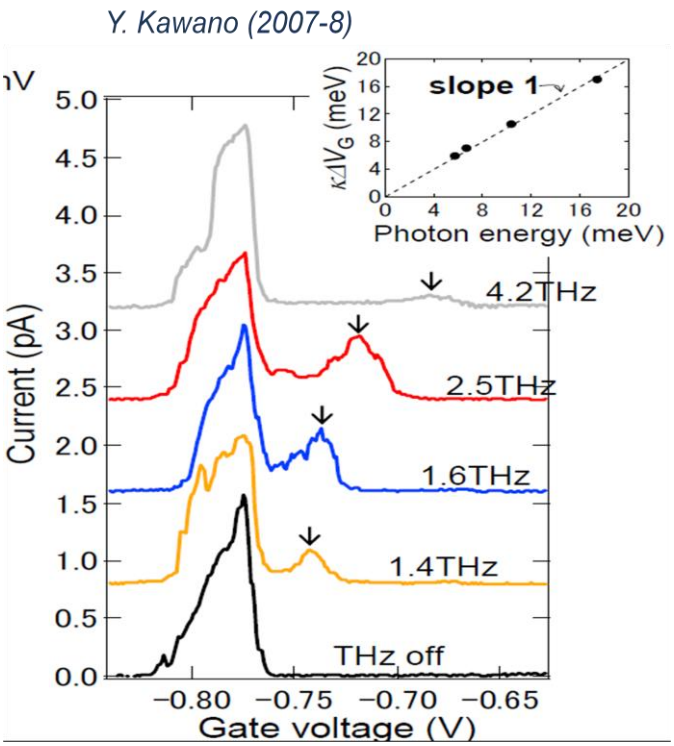

Fig. 2. (a) Experimental data by Y. Kawano et al. (see Refs. [35-37]). That group used semiconducting carbon nanotube junctions serving as a quantum well with the single electron tunneling. Their devices detect weak THz fields having minimal power as low as ~1 fW in the frequency range 1-5 THz. The plots above illustrate evolution of the single electron tunneling resonances under the THz irradiation.

The authors of Refs. [35-37] fabricated and tested the carbon nanotube quantum wells which exploit principles the photon-assisted single electron tunneling. Their devices detect the external electromagnetic field signals as weak as ~1 fW in the frequency diapason 1-5 THz. Nevertheless the available spectral range obtained in works [35-37] is too narrow while their working temperature $T \leq 10\,\mathrm{K}$ is too low yet for many practical purposes. Therefore our work aimed at extending of the carbon nanotube sensor capabilities. We studied possibilities to widen the multispectral analyzer frequency diapason, to reduce the noise level, and to improve the detector sensitivity.

Our research findings

1. Sensing an electromagnetic field with photon-assisted Fano resonance in a two-branch carbon nanotube junction.

A Fano electromagnetic field sensor

In a typical setup one measures [2-6,8,A-D] changes of electrical characteristics of a single wall

carbon nanotube (SWCNT) section C attached to normal metal electrodes N_1 and N_2 (see the sketch in Fig. 3a where V_{SD} denotes the source-drain bias voltage and V_G is the gate voltage), which constitutes the nanotube junction (NJ). The NJs of various configurations are subject to extensive experimental and theoretical study [2-6,8,A-D]. In Fig. 3 the nanotube C resides on the substrate S and is coupled to the N electrodes via the Schottky barriers I arising due to differences of electron concentrations in C and $N_{1,2}$. Because electron motion in the C section is quantized [9], the carbon nanotube junctions is quoted as a one-dimensional (1D) quantum dot. The quantized states formed inside the dot cause various resonances experimentally observed in transport characteristics of the carbon nanotube junctions [1,2,5,6,8,9,10] and quantum dots [10,41]. A steady state quantum interference between localized electron states in C and continuum states in N electrodes results in sharp Fano peaks and dips pronounced in the electron transport characteristics [5,6,8,9] of the NJ nanodevices.

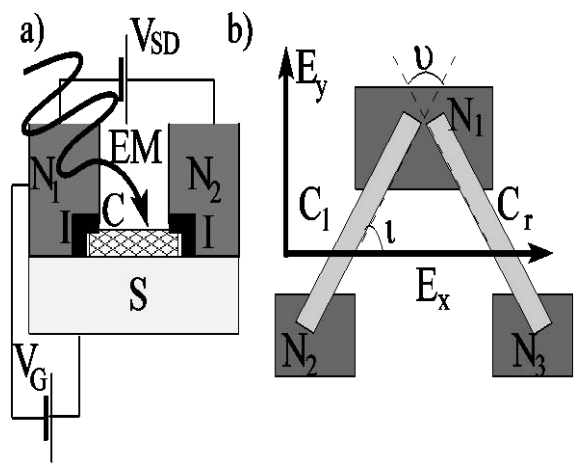

Fig. 3. (a) A carbon nanotube junction (NJ). (b) A Λ-sensor of the EF with electric field components E_x and E_y.

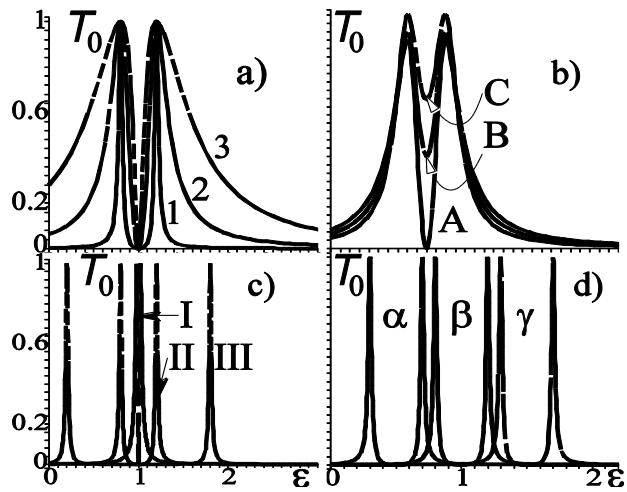

Fig. 4. The stationary transmission coefficient T_ε: (a) for different magnitude of the linewidth Γ; (b) for various field polarizations; (c) for various level energy differences Δ; and (d) for various total level energies $\bar{\varepsilon}$.

In this part of work we studied the influence of an external electromagnetic field (EF) on the Fano resonance in an carbon nanotube junction. We will see that an external electromagnetic field induces photon-assisted tunneling processes across the nanotube junction. This strongly affects sharp quantum mechanical resonances taking place in the nanotube junction. The 1D nature of the electron transport in SWCNT is exploited to determine polarization of the electromagnetic filed. The above phenomenon is suggested for sensing an external THz signals.

Theoretical model

We consider a two-branch carbon nanotube junction exposed to an external EF. The junction is composed of carbon nanotube sections $C_{l(r)}$ coupled to metallic electrodes $N_{1,2,3}$ via electron tunneling. Quantum interference between localized electron states in the carbon nanotube branches and continuum states in the metallic electrodes causes sharp Fano resonances. The sharp peaks are affected by an external a.c. field which induces tunneling processes accompanied by emission and absorption of photons. We will see that the photon-assisted tunneling results in appearance of satellite peaks in addition to the main Fano resonance. In this paper we implement an illustrative and tractable model, which describes the photon-assisted phase-coherent electron transport across a two-branch SWCNT junction. Despite its simplicity, our model adequately captures basic physical features of photon-assisted electron transport under the conditions of the Fano resonance. The SWCNT branches $C_{l(r)}$ are presumed to be "clean", which implies that the

electron movement is ballistic ($l_i \geq L_{l(r)}$, where l_i is the electron elastic mean free path and $L_{l(r)}$ is the length of the nanotube section). The $C_{l(r)}$ branches are misaligned by angle ϑ and are coupled to each other indirectly via the common normal metal electrode N_1, as shown in Fig. 3b.

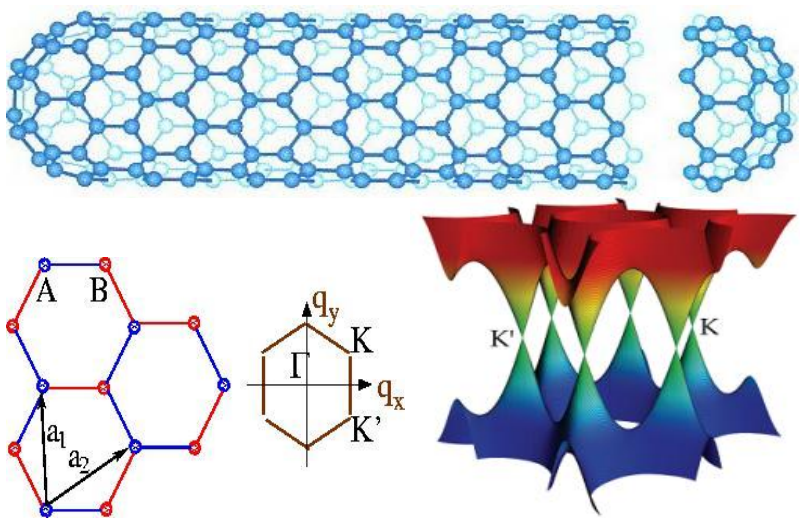

Fig. 5. A section of carbon nanotube, its crystal lattice structure, a Brilloin zone, and the 3d plot of electron energy versus momentum.

The Λ-shape of the nanosensor pursues a double purpose: (*i*) one measures the d.c. conductivity $G(V_{SD}, V_G)$ in each of the C sections independently; (*ii*) the 1D nature of electron transport in the C sections allows simultaneous independent measurement of components E_x and E_y (see Fig. 3b) of the external electromagnetic field. The finite misalignment angle ϑ assures that the a.c. bias $V_{ac}^{l(r),t(b)}$ [here indexes $l(r)$ refer to the left (right) branches of the Λ-sensor, while the indexes $t(b)$ are related to the top (bottom) Schottky barriers] is induced on the NJ's Schottky barriers by a certain projection of the electric field vector $\mathbf{E} = E_x\hat{x} + E_y\hat{y}$.

In the geometry of Fig. 3b one obtains $V_{ac}^{l,t(b)} \propto E_x \sin\theta + E_y \cos\theta$ and $V_{ac}^{r,t(b)} \propto -E_x \sin(\theta + \iota) - E_y \cos(\theta + \iota)$. An arbitrary EF polarization $V_{ac}^{l,t(b)} \neq V_{ac}^{r,t(b)}$ gives different probabilities of elementary photon-assisted tunneling in each of the two branches C_l and C_r.

The inter-level spacing is estimated as $\delta\varepsilon = hv_F / 2L$ [where v_F is the Fermi velocity in the carbon nanotube, $v_F \simeq 8 \times 10^5$ m/s, and L is the nanotube length, $L = 2 \times (10^2 - 10^3)$ nm]. The level energies ε_i are controlled by changing the charge carrier concentration when applying the gate voltages V_G^i to C_i. Since only one level ε_i supports the transport across the i-th dot (if either the inter-level spacing $\delta\varepsilon$ or the level energy difference Δ is larger than the bias voltages V_{SD} and V_G, linewidth Γ, and temperature T), no intradot Coulomb interaction is present. In this way one neglects the charge accumulation on the nanotube sections, and accounts just for one type of the carriers. This is justified when $\max\{\Gamma, e^2 / 2C\} << \min\{\delta\epsilon, \Delta\}$, i.e., when electron propagation inside the C-sections is well

quantized and the NJ capacitance C is not small. Though the above assumption is very simple, it allows deriving of tractable analytical expressions, which appears to be quite convenient for a qualitative and quantitative analysis.

Photon-assisted Fano resonance

For the sake of simplicity, we ignore the dependence of the tunneling matrix elements t_{si} versus the energy variable ε and electron momentum $\mathbf{p}$. Besides, we assume that the tunneling matrix element t_{si} is the same for all the junctions, i.e., $|t_{si}| = |t|$. Due to electron scattering on atomic defects and tunneling with rates $\Gamma_{\mathbf{i}}$ and Γ_s respectively, the dot energy levels acquire a finite linewidth $\Gamma_{\mathbf{i}} + \Gamma_s$, where $\Gamma_s = 2\pi|t|N_s(0)$, and $N_s(0)$ is the density of states in the s-th N lead. Our model assumes no direct interaction (neither Coulomb repulsion, nor tunnel coupling) between the sections C_l and C_r. The steady quantized states are coupled to each other rather indirectly via continuum electron states in the N leads. We will see that a finite external electromagnetic field produces series of sharp satellite singularities, which arise in the $G(V_{\mathbf{SD}})$-curves in addition to the steady state resonances. The position and magnitude of the satellite singularities, which constitute the photon-assisted Fano resonance, are uniquely related to the parameters of the external electromagnetic field.

Our calculation results for the steady state transmission coefficient $\mathcal{T}_0(\varepsilon)$ are presented in Fig. 4a-d. In Fig. 4a we plot $\mathcal{T}_0(\varepsilon)$ for $\beta_l = \beta_r = 1$, $\bar{\varepsilon} = 1$, $\Delta = 0.2$, $\Gamma = 0.05$ (curve 1), $\Gamma = 0.25$ (curve 2), and $\Gamma = 0.6$ (curve 3). One can see that $\mathcal{T}_0(\varepsilon)$ vanishes at $\varepsilon = \bar{\varepsilon}$. One may also notice a well-pronounced double-peak singularity affected by asymmetry of the setup. The transmission becomes ideal [i.e., $\mathcal{T}_0(\varepsilon) = 1$] at $\varepsilon = \bar{\varepsilon} = \Delta$. Fig. 4b illustrates the effect of transmission asymmetry when $\beta_l^t \neq \beta_r^b$. All the parameters used for calculations in Fig. 4b are the same as in the former Fig. 4a except $\Gamma = 0.3$ and $\beta_r = 0.01$ (curve A), $\beta_r = 0.5$ (curve B), and $\beta_r = 1$ (curve C). In Fig. 4c we show $\mathcal{T}_0(\varepsilon)$ for various level energy differences $\Delta = 0.02$ (curve I), $\Delta = 0.2$ (curve II), $\Delta = 0.8$ (curve III). All other parameters are the same as before. In Fig. 4d we plot $\mathcal{T}_0(\varepsilon)$ for different values of the sum level energy $\bar{\varepsilon} = 0.5$ (curve α), $\bar{\varepsilon} = 1$ (curve β), and $\bar{\varepsilon} = 1.5$ (curve γ). The partial transmission coefficient $\mathcal{T}_m(\varepsilon)$ for an arbitrary m-photon-assisted process is obtained from $\mathcal{T}_0(\varepsilon)$ with shifting the energy argument by $m\hbar\Omega$.

The calculation results for the Λ-sensor conductivity G versus the source-drain bias voltage $V_{\mathbf{SD}}$ (in units of $\bar{\varepsilon}$) are shown in Fig. 6. For the sake of simplicity, we assume that the a.c. and d.c. biases are the same for all the Schottky barriers, which is the case for a symmetric NJ and $E_x = E_y$. Then, in all the equations one sets $V_{\mathbf{ac}}^{l(r),t(b)} = V_{\mathbf{ac}}$ and $V_{\mathbf{SD}}^{l(r),t(b)} = V_{\mathbf{SD}}$. Fig. 6a shows the Λ-sensor conductivity for $eV_{\mathbf{ac}} = 0.1$ (curve 1), $eV_{\mathbf{ac}} = 0.2$ (curve 2), and $eV_{\mathbf{ac}} = 0.5$ (curve 3). Other relevant parameters are $\beta_l = 1$, $\beta_r = 1$, $\bar{\varepsilon} = 1$, $\Delta = 0.07$, $\Gamma = 0.03$, and $\Omega = 0.4$. One can see that the a.c. EF induces series of satellite double-peak singularities, with positions and relative amplitudes depending on the EF intensity. When the intensity of the external EF is low, the photon-assisted tunneling signatures are weak: only a weak double-peak singularity appears at the bias voltages $V_{\mathbf{SD}} = (\bar{\varepsilon} \pm (\Omega + \Delta))/e$ [see curve 1]. Splitting between the main peak and the first adjacent satellite peak in this case is $\hbar\Omega/e$. However, as the a.c. field amplitude $E_{\mathbf{ac}}$ increases, the amplitude of the main peak decreases

while the satellite double-peaks become much sharper (see curves 2 and 3). We emphasize that here we neglected the non-equilibrium effects despite the a.c. field is strong. This is justified since $\Omega\tau_\epsilon << \hbar$. The Λ -sensor conductivity at different Ω is presented in Fig. 5b, where curve A corresponds to $\Omega = 0.1$; curve B to $\Omega = 0.4$, and curve C to $\Omega = 0.7$. Other relevant parameters are $\beta_l = \beta_r = 1$, $eV_{\mathbf{ac}} = 0.3$, $\bar{\varepsilon} = 1$, $\Delta = 0.07$, and $\Gamma = 0.03$.

Frequency range and sensitivity.

Using the above data one may summarize the EF sensing method as follows: (*i*) the electromagnetic field frequency is readily extracted from splitting of the double peak structure (Fig. 5a); (*ii*) the field vector components $E_{x,y}$ (see Fig. 3b) are determined by the ratios of the main and the satellite double peak heights; (*iii*) field polarization is obtained by comparing the satellite peak heights in the conductivities G_l and G_r of the two adjacent NJ branches. One utilizes the fact that an arbitrary EF polarization gives different sequences of peak heights in $G_{l,r}$ of the two NJ branches l and r. From a measurement, one determines ratios of the main and the satellite double peak heights κ_μ for each of the branches $\mu = x, y$. Then, one finds $E_{x,y}$ from two transcendental equations $J_1^2(\alpha_\mu) / J_0^2(\alpha_\mu) = \kappa_\mu$, where $\mu = x, y$. The $\hat{x}$ - and $\hat{y}$ -components of the a.c. electromagnetic field vector $\mathbf{E}$ are readily obtained from the universal dependence $\alpha(\kappa_{x,y})$. The function $\alpha(\kappa_\mu)$ [where $\varphi = \arctan(\kappa_x / \kappa_y)$] is given in Fig. 6c.

The sensitivity diagram in Fig. 6c is obtained for $\omega_{\mathbf{D}} = 10$, $\lambda = 0.3$, $p_{\mathbf{F}} = 1$, $k_{\mathbf{D}} = 1$, $\Delta = 1$. One can see that the temperature broadening due to coupling of electrons to phonons significantly restricts sensitivity of the Fano nanosensor at high frequencies (which for the used carbon nanotube junction parameters are below 1.7 - 17 THz) and temperatures $T \geq 7\Delta$ (which corresponds to 80-800 K for the same device parameters). The above calculations were made under the assumption that the external field amplitude is weak. We have actually disregarded non-equilibrium effects along with the changes in the electron bandstructure due to the photon-assisted tunneling. However, the above assumptions become invalid if the electromagnetic field is strong. In the latter case, the non-equilibrium phenomena influence the nanosensor characteristics substantially. Strong electromagnetic field changes the electron distribution function f_ε, affecting electron transport across the NJ directly. Besides, if the C section is longer than the electron diffusion length, it causes instability in respect to the appearance of inhomogeneous regions along C. In an experiment one may use SWCNT as the left (right) shoulders $C_{\mathbf{l(r)}}$ and Pd as the N leads. The stationary Fano resonance is tuned by applying the gate voltages $V_{\mathbf{G}}^{l(r)}$ to get an optimal value of Δ. The gate voltage influence is understood when one considers that the inter-level energy spacing $\delta\varepsilon = hv_{\mathbf{F}} / 2L$ depends on the Fermi velocity $v_{\mathbf{F}} = (\hbar / m^*)(3\pi^2 n)^{1/3}$. The electron effective mass m^* and the electron concentration n both can be tuned by applying appropriate gate voltages. The electron carrier concentration is altered by the gate voltage $V_{\mathbf{G}}$ applied to the nanotube junction in the way [5,6,8,9] as shown in Fig. 3a. The effective electron mass is controlled using the split-gate configuration. The split gate voltage $V_{\mathbf{SG}}$ affects the electron bandstructure of a "helical" nanotube already at $E \geq 10$ V/μ m (1 mV/Å). Other types of semiconducting nanotubes (e.g., zigzag) require stronger fields (≥ 0.2 V/Å) to induce a metal-semiconducting transition when a finite energy gap is opened in the electron excitation spectrum. For typical lengths

$L_{\mathbf{l(r)}} = 0.2 - 2$ μm of $C_{\mathbf{l(r)}}$, one finds that $\Delta = 1 - 10$ meV (0.24-2.4 THz). At these parameters, the Λ-sensor works in the THz frequency range at temperatures $T = 1 - 100$ K. A correspondence between the field intensity and $V_{\mathbf{ac}}^{l(r),t(b)}$ is obtained from a self-consistent numeric solution of Maxwell equations, completed by equations for electron spectrum, conductance, junction transmission, and the plot in Fig. 5c addressing the particular setup. Verification is made using calibrating measurements. In this way, the photon-assisted Fano resonance in the Λ-shaped junctions allows to determine the external electromagnetic field parameters.

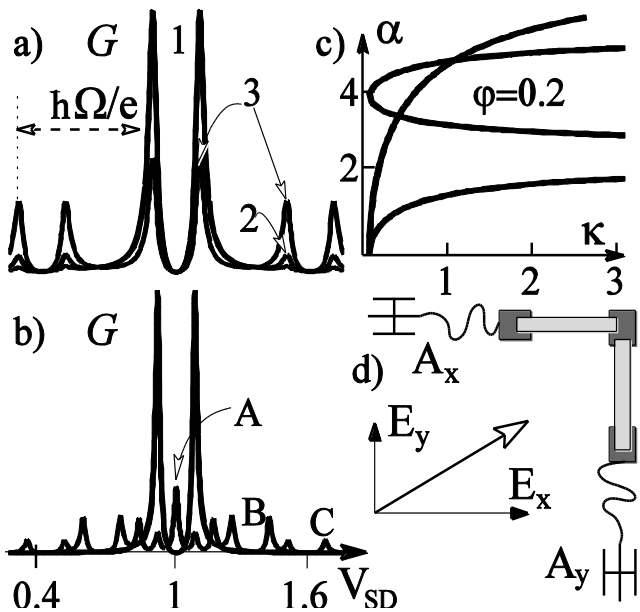

Fig. 6. Calculation results for the linear conductivity $G(V_{SD})$ of the Λ-sensor. (a) The $G(V_{SD})$ -curves for three different external EF amplitudes V_{ac}. The splitting between the satellite peaks is $\propto \hbar\Omega / e$. (b) $G(V_{SD})$ for three different field frequencies. (c) The universal dependence $\alpha = eV_{ac}/\Omega$ versus $\kappa = J_1^2(\alpha)/J_0^2(\alpha)$ where J_n is the Bessel function of order n. (d) The Λ-nanosensor with antennas attached to the NJ-branches.

Indeed, the sketch in Fig. 3b is idealized. If the a.c field frequency is comparable to c / L, one needs no external antenna, since one may utilize the intrinsic antenna effect observed and described in Refs. [A] (see also references there in). However, if the a.c. frequencies lay well below c / L, i.e., when the EF wavelength becomes much shorter than the nanotube length, one needs an additional external antenna as schematically shown in Fig. 6d. By attaching external antennas, one improves the reception of electromagnetic signals if the electromagnetic field wavelength and the nanotube length do not match each other. The external antennas may be fabricated using lithography methods. Then they are electrically connected to the metallic electrodes of the Λ-junctions. In the geometry of Fig. 6d, the a.c. field components E_x and E_y are tuned independently by each of the antennas, and are transmitted to the corresponding branch of the Λ-junction.

The frequency range of the Λ-sensor is determined by several factors. Along with the circuit noises and influence of the external environment, there are intrinsic sources of noise. They originate from temperature broadening Γ of the Fano resonance peaks due to the electron-phonon coupling discussed in previous subsection. The magnitude of Γ depends on the temperature and on the coupling strength between the SWCNT sections and metallic electrodes. Another fraction of broadening is due to coupling of the nanotube to metallic electrodes. That mechanism depends mostly on the transparency of the Schottky barrier. The net broadening is also determined by the quality of interfaces and by the purity of the electrodes.

Besides the broadening, one should also account for positions of the quantized energy levels ε_n and for the inter-level spacing Δ. Both of them, ε_n and Δ, depend on the length of the SWCNT sections. The relevant frequency range corresponds to the THz domain ($\Delta\nu_{\mathrm{EF}} = 0.5$-50 THz, or, in terms of wavelength, $\lambda_{\mathrm{EF}} = 1$ mm-5 μm). This means that the EF wavelength

and the nanotube section size match each other just for shortest waves of the THz domain only. The range $\Delta\nu_{\mathrm{EF}}$ is limited by circuit parameters and by coupling to the external environment. Besides, there are additional restrictions having an intrinsic origin, as discussed in former section. The upper frequency limit (i.e. shortest wavelengths) is determined by maximal level energy difference Δ. The lower frequency limit depends upon coupling between the nanotube shoulders and the broadening due to electron-phonon interaction. The inter-electrode coupling depends on several factors including transparency and geometry of the Schottky barriers, and also purity of the normal electrodes. Since the elastic electron scattering on the atomic defects and on the adsorbed molecules (which stick to the nanotube sections[2-6]) contributes into the localized level width, it also affects the lower frequency limit (i.e., the frequency resolution of the nanosensor).

Our work suggests that the carbon nanotube sensors have numerous advantages as compared to other types of devices. One important benefit is that the intrinsic properties of the nanotube sections are controlled by gate and source-drain bias voltages [5,6,8,9]. In this way, one alters the electron bandstructure and/or the charge carrier concentration. The electron bandstructure is affected by a transversal electric field [A-D] in a split gate configuration. Typical magnitudes of the electric field may be quite low [$E \geq 10$ V/μ m or 1 mV/Å for a particular class of 'helical' (n,1) nanotubes], or 0.01-1 V for other types of semiconducting nanotubes [5,6,8,9]. The charge carrier concentration and frequencies of quantum mechanical resonances are changed under the influence of a bias gate voltage [5,6,8,9]. Using the d.c. bias voltages V_{SD} and V_{G}, one insures perfect tuning of the carbon nanotube sensors as well as a prompt optimization of their working characteristics. Another advantage of NJs is presence of sharp intrinsic resonances in their transport characteristics. For such reasons the carbon nanotube sensors may be easily tunable and work with a good precision.

2. Probing the intrinsic state of a one-dimensional quantum well with a photon-assisted tunneling.

The THz diapason of the carbon nanotube spectral analyzers can be extended by fabricating of combs the metallic carbon nanotubes. The metallic nanotube combs sould be combined with the semiconducting nanotube combs as shown schematically in Fig. 1. The metallic nanotube combs are furnished of single wall carbon nanotubes laid on a dielectric substrate. Each of the individual junctions in the comb consists of the single wall metallic nanotube $\mathcal{T}$ with emitter ϵ and collector $\mathcal{C}$ electrodes attached to its ends (see sketch of a single junction in Fig. 7). The junction infact furnishes a quantum well with quantized energy levels formed inside. Depending on the tube properties, that setup (see Fig. 7) corresponds to various condensed matter systems. The single wall carbon $[n,m]$ tube sketched in Fig. 5 is a rolled up atomic honeycomb monolayer formed by two sublattices A and B. The integer indexes n and m ($n \geq m \geq 0$) of the rollup vector $\mathbf{R} = n\mathbf{R}_1 + m\mathbf{R}_2$ actually determine the electronic bandstructure of the tube. In particular, if $n - m = 3\nu$ (ν being an integer) the tube is metallic while it is semiconducting or insulating otherwise [11]. The charge carriers in metallic tubes conform to the linear dispersion law $\varepsilon_k = \pm v_{\mathbf{F}} \left|\mathbf{k}\right|$ [where " $\pm$ " corresponds to electrons (holes), and $v_{\mathbf{F}}$ is the Fermi velocity]. A lot of discussions address the intrinsic state of metallic tubes where the Tomonaga Luttinger liquid state [14] (TLL) may presumably occur [12,13,15,16,17]. In contrast to semiconducting tubes, where a general consensus is achieved, unconventional features of the metallic tubes are not well understood yet. A lot of attention [12,13,15,16,17] is paid to the strong correlation effects, and to the one-dimensional transport of the electric charge carriers. Along with the TLL state [14] in metallic tubes [12,13,15,16,17] under the current elaboration there are models operating with non-interacting electrons while other models exploit coupling of the tube to the external environment[18]. Although there are indications of the TLL state in the shot noise[15] and in angle integrated photoemission measurements[16], present experimental

evidences are still indirect[18,19]. Therefore more efforts to clearly identify the intrinsic state of the one-dimensional quantum wells formed of metallic carbon tubes are required.

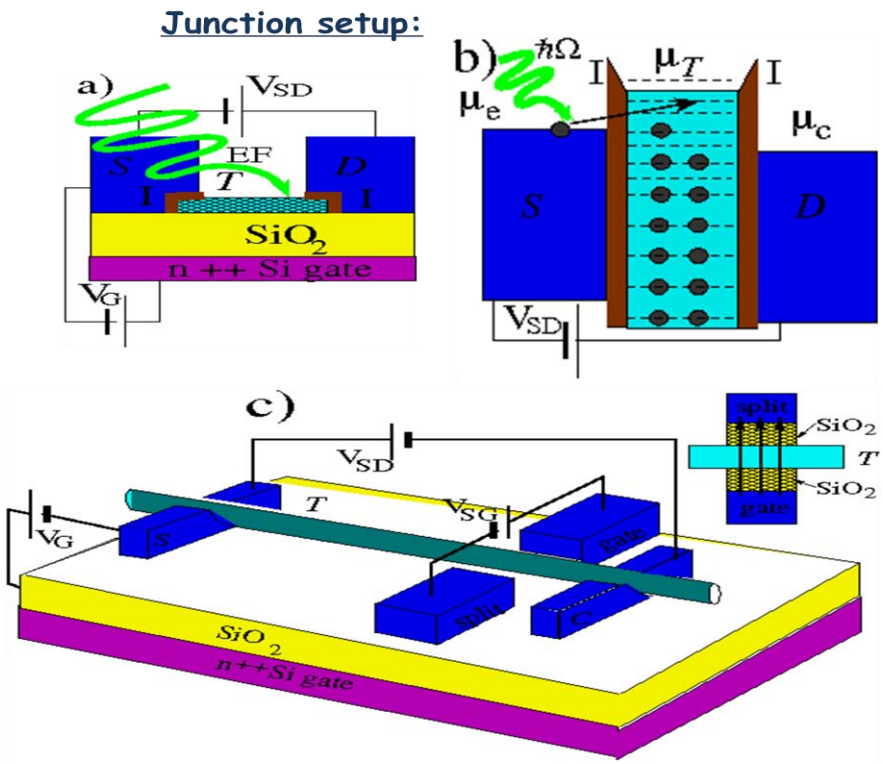

Fig. 7. (a) A quantum well (QW) composed of the 1D section $\mathfrak{T}$ with emitter $\mathfrak{E}$ and collector $\mathfrak{C}$ electrodes attached. The potential barriers are shown in black at the $\mathfrak{E}/\mathfrak{T}$ and $\mathfrak{T}/\mathfrak{C}$ interfaces. (b) Energy diagram of the PAT process in the QW. (c) The split gate configuration of the QW. The right side inset shows how the electric field is applied to the $\mathfrak{T}$ section.

Typical quantum well setup [5,6,B-D] is sketched in Fig. 7 where the 1D section is denoted as $\mathcal{T}$. The bias voltage $V_{\rm ec}$ drops between the emitter (ϵ) and collector ($\mathcal{C}$) electrodes, while the gate voltage $V_{\rm G}$ is applied to the n ++Si substrate as shown in Fig. 7. The electrochemical potentials in ϵ, $\mathcal{T}$, and $\mathcal{C}$ are denoted as $\mu_{e,T,c}$. The ϵ and $\mathcal{C}$ electrodes are separated from the metallic tube section $\mathcal{T}$ by the interface barriers I shown in black in Fig. 7 (a,b). The potential barriers emerge from differences between the Fermi velocities in the adjacent electrodes. In this part of work we suggest a method which identifies the quantized levels of charge and spin excitations in the Tomonaga Luttinger liquid state inside the 1D quantum well shown in Fig. 7(a-c). Our method exploits the fact that the electromagnetic field (EF) interacts with the charge excitations only, while the neutral particles remain unaffected. When a tunneling electron with energy ε absorbs n photons of the external electromagnetic field, the intrinsic structure of the TLL state in $\mathcal{T}$ is pronounced in the multiphoton tunneling process probability. The photon-assisted tunneling (PAT) influences probability of the single electron tunneling (SET) which helps to elucidate the intrinsic state of the tube. In this paper we address quantum wells with long and short $\mathcal{T}$ sections. When the tube is long, the interlevel spacing $\Delta = hv_{\rm F} / L$ ($v_{\rm F}$ is the Fermi velocity, L is the tube length) is small. Therefore quantization of the electron motion inside $\mathcal{T}$ is negligible. In that case the local single electron density of states $\mathcal{N}(\varepsilon)$ inside $\mathcal{T}$ has a dip at zero energy $\varepsilon = 0$. We will see that such a dip is clearly visible in the photon-assisted and in the single electron tunneling characteristics which helps to identify the TLL state. In the opposite limit when the tube is short, the ballistic motion of the charged and neutral excitations inside $\mathcal{T}$ is quantized. During the tunneling, an electron splits into four $\rho_{\pm},\sigma_{\pm}$ -bosons (two density and two spin). The bosons populate quantized levels with different energies $\varepsilon_{\rho+} \neq \varepsilon_{\rho-(\sigma\pm)}$.

The charge boson energy levels are detected with the photon-assisted tunneling (PAT, see Ref. [B]). We will see that the tunneling mechanism is sensitive to the emitter-collector $V_{\mathbf{ec}}$ and the gate $V_{\mathbf{G}}$ voltages. Therefore the TLL properties are pronounced in the differential conductivity curves of the one-dimensional quantum wells. In measurements made on the same setup, the spin boson levels are fingered from Zeeman splitting $\propto \mu_{\mathbf{B}} H / e$ when applying a finite d.c. magnetic field $H \neq 0$. The quantization of both the charge and spin excitations is proclaimed in the differential conductivity curves of the quantum well.

The TLL tunneling density of states of a long QW

If the metallic tube section $\mathcal{T}$ is long, $L > v_{\mathbf{F}} \tau_{\mathbf{T}}$ (where $\tau_{\mathbf{T}} = \hbar / \Gamma_n$ is the net tunneling time), the quantization inside $\mathcal{T}$ is negligible. The level separation for typical carbon tube junctions [5,6,8-10] becomes indistinguishable when $L \geq 3$ μm. Strong electron correlations drive the electron system into the *Tomonaga Luttinger liquid* (TLL) state[12-19].

A simple evaluation from the bandstructure calculations gives $\beta_{\mathbf{G}} = 0.005 - 0.03$ depending on directions of the rollup vector $\mathbf{R}$. The $\mathcal{N}(E)$ shape is also controlled with $V_{\mathbf{SG}}$ utilizing the split gate configuration [A-C] as shown in Fig. 7(c). The electric field in that setup is perpendicular to the tube axis as shown in the right inset to Fig. 7(c). The split-gate setup allows driving the tube electron state from semiconducting to the metallic one. The transversal electric field induces a finite dipole momentum directed in perpendicular to the tube, which renormalizes g as well.

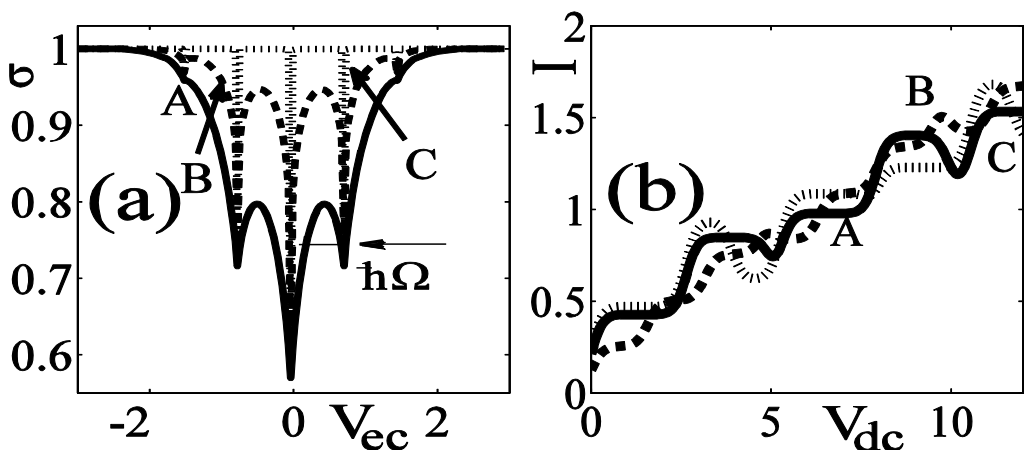

Fig. 8. (a) (a) Splitting of the zero-bias TLL dip in the differential tunneling conductivity $\sigma(V_{ec})$ [in units of e^2 v_F N(0)] in a long CNT junction due to the photon-assisted tunneling. Spacing between the zero dip and adjacent satellite dips is $\hbar\Omega / e$. (b)The Coulomb staircase in the PASET current-voltage characteristics $I(V_{dc})$ versus reduced voltage V_{dc} (see text) of the CNT junction in the TLL state with g=0.4 under influence of the a.c. bias field with the amplitude $eV^{(1)}$=3.4 (in units of $\delta = e^2/C$) and for a symmetric junction (η = 0.5). Curve A corresponds to Ω = 4.7, curve B to Ω = 3.7 and curve C to Ω = 6.7.

The corresponding alteration of the Luttinger parameter g is evaluated using, e.g., results of Refs. [27-29]. It gives $g \to g \cdot J_0^{-1}\left(V_{\mathbf{SG}} d / \hbar v_{\mathbf{F}}\right)$. For a narrow-gap semiconducting $\mathcal{T}$ (see Ref. [30]) and for typical parameters of the tube quantum well, the split gate induced change is $g \to g + \beta_{\mathbf{SG}} V_{\mathbf{SG}}$ where $\beta_{\mathbf{SG}} = 0.01 - 0.05$ for different rollup vectors. If the transversal electric field $V_{\mathbf{SG}} / d$ inside $\mathcal{T}$ is sufficiently strong, one induces a semiconducting-metal

transition [27-29]. The electronic properties of the tube then switch from a one-dimensional narrow gap semiconductor to the TLL. The time-averaged conductance $\sigma(V_{\mathbf{ec}})$ of the long CNT junction exposed to an external electromagnetic field is computed using Maxwell equations combined with the Green function approach. We compute $\sigma(V_{\mathbf{ec}})$ and the electric current $I(V_{\mathbf{dc}})$ [$V_{\mathbf{dc}} = (V_{\mathbf{ec}} - V_t)\eta$ is the reduced voltage, $V_t = (E - \epsilon_{\mathbf{F}}) / e\eta$ is the SET threshold voltage] for the two cases of interest. One limit corresponds to $\delta << \mathcal{T}$ when the single-electron tunneling is not essential [$\delta = e^2 / C$, $C = C_e + C_c$ is the net capacitance of the double-barrier junction, $C_{e(c)}$ is the emitter (collector) capacitance]. The current-voltage characteristics $I(V_{\mathbf{dc}})$ [where $V_{\mathbf{dc}} = (V_{\mathbf{ec}} - V_t)\eta$] in condition of the photon-assisted single-electron tunneling (PASET) across the quantum well in the Tomonaga Luttinger liquid state are shown in Fig. 8(b). According to Ref. [23], the equilibrium shape of the $I(V_{\mathbf{dc}})$ curves (quoted as Coulomb staircase) is extremely sensitive to the double-barrier junction's parameters such as barrier transparencies, capacitance, symmetry, purity of the carbon tube section, and the energy level spacing. The photon-assisted tunneling induced by the external electromagnetic field introduces additional features in those curves. We have computed PASET curves for a QW with a long $\mathcal{T}$ -section where the single electron tunneling takes place. The external $\hat{x}$ -polarized electromagnetic field induces an a.c. bias voltage across the junction as $V^{(1)} \cos \Omega t$. The most remarkable elements of the $I(V_{\mathbf{dc}})$ curves A-C in Fig. 8(b) are local dips which originate from an interference between the zero-energy TLL anomaly pronounced in equilibrium at $\varepsilon = 0$ [see Fig. 8(a)] and the photon-assisted single electron tunneling processes. The Coulomb staircase curve A in Fig. 8(b) corresponds to $\Omega = 4.7$, curve B to $\Omega = 3.7$ and curve C to $\Omega = 6.7$ computed for $g = 0.4$.

Identifying of the charge and the spin boson energy levels

In a opposite limit when the $\mathcal{T}$ -section is short, the quantized energy levels are well resolved, since the condition $\Gamma^{e,c} << \Delta$ is observed ($\Gamma^{e,c}$ are the $\epsilon \Leftrightarrow \mathcal{T}$ and $\mathcal{T} \Leftrightarrow \mathcal{C}$ electron tunneling rates, $\Delta = hv_{\mathbf{F}} / L$ is the interlevel spacing inside $\mathcal{T}$). In this Section we neglect by the single-electron tunneling (SET) contribution [23] (Coulomb blockade phenomena). That is justified when the temperature T is not too low, $T >> \Gamma^{e,c}$. In that limit we use equation for electric current again but with a different spectral density function $\mathbf{Im}\mathcal{K}(\varepsilon)$ which now acquires a comb-like shape. Due to the spin-charge separation in the Tomonaga Luttinger liquid (TLL) there are two sets of quantized energy levels in a low-transparent quantum well with a short $\mathcal{T}$ -section. For the QW transparency $\tilde{T} = 0.3$ (where $\tilde{T} = 4\pi\Gamma_n L_n / (\hbar v_F)$, $L_n = L_e + L_c$, L_e and L_c are the ϵ and $\mathcal{C}$ thicknesses respectively, $v_F = 8.1 \cdot 10^5$ m/s) one gets $\Gamma_n \approx 0.3$ meV. For the tube length $L = 3$ μm one obtains spacing between the quantized levels as $\Delta = 1$ meV. The photon-assisted processes cause an additional splitting ~0.6 meV which corresponds to the a.c. bias frequency $\Omega \approx 1$ THz. Following to Refs. [12,22], one defines the transmission coefficient as $\tilde{T}(E) = | i\hbar G^R \left(L, E \right) |^2$. We assume that coupling of the single wall tube segment $\mathcal{T}$ to the external ϵ and $\mathcal{C}$ electrodes is weak. In this approximation we compute the local electron density of states $\mathcal{N}(\varepsilon)$ implementing boundary conditions [12] for the electron wavefunction inside a short carbon tube section $\mathcal{T}$. Then the quantized energy levels are firmly separated from each other and resolved. The charge ρ_+ bosons populate the energy levels $\varepsilon_n^{\rho+} = hv_F n / Lg = n\Delta / g$ (where n is integer number), while three other neutral ρ_-

and $\sigma_{\pm}$ -boson energy levels have conventional values $\varepsilon_n^{\rho-(\sigma\pm)} = hv_F n / L = n \cdot \Delta$. In the steady state, when the EF is off (i.e., $\alpha_{\mathbf{ec}} \equiv 0$), during the tunneling say, from ϵ to $\mathcal{T}$, an electron splits into four bosons as $e \to \rho_+ + \rho_- + \sigma_+ + \sigma_-$, which assumes the energy conservation as $E + \eta e V_{\mathbf{ec}} = \varepsilon_n^{\rho+} + \varepsilon_n^{\rho-} + \varepsilon_n^{\sigma+} + \varepsilon_n^{\sigma-} = n\left(3 + 1/g\right)\Delta$ (n being the integer number). That corresponds to a resonance tunneling through the quantized TLL states tuned by $V_{\mathbf{ec}}$. However, if the electromagnetic field (EF) is on ($\alpha_{\mathbf{e,c}} \neq 0$), the resonance tunneling condition changes. That happens because the a.c. field acts on the charge ρ_+ -bosons only, which absorb the EF photons during the photon-assisted tunneling processes.

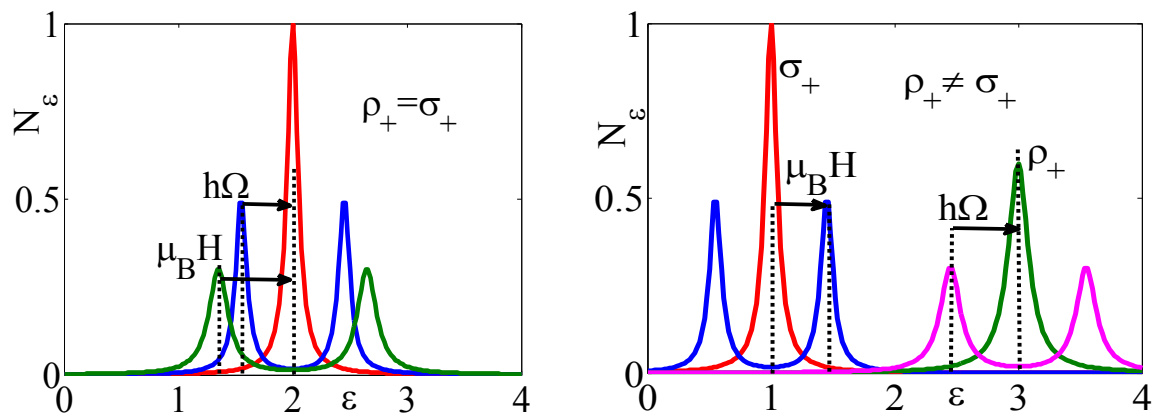

Fig. 9. Splitting of quantized levels due to the photon assisted tunneling and Zeeman effect as pronounced in the single electron density of states N(ε) of a short CNT junction. (a) A free electron quantized level (solid curve) for which the charge ρ_+ and spin σ_+ bosons coincide splits by an a.c. electromagnetic field (with spacing $\propto \hbar\Omega / e$) and by a d.c. magnetic field (with spacing $\propto \mu_B H / e$) simultaneously. (b) The quantized levels of spin σ_+ and charge ρ_+ bosons have different energies $\varepsilon_n^{\rho+} \neq \varepsilon_n^{\sigma+}$ in the TLL state. The a.c. bias splits the charge boson levels (dashed curve on the right) while the d.c. magnetic field splits the spin boson levels (dotted curve on the left) only. The charge boson localized energy level $\varepsilon_n^{\rho+}$ splits in the two satellite peaks with spacing $2\hbar\Omega / e$. Although the a.c. field has no influence to the neutral spin bosons, the spin level $\varepsilon_n^{\sigma+}$ splits [12] in two sublevels spaced with $\Delta_Z \propto \mu_B H / e$ (both in units of Δ) due to the Zeeman effect when a d.c. magnetic field $H \neq 0$ is applied.

The photons do not excite the neutral ρ_- and $\sigma_{\pm}$ bosons since they do not interact with the external electromagnetic field. The a.c. field-modified resonance condition depends on both $V_{\mathbf{ec}}$ and Ω simultaneously $E + \eta e V_{\mathbf{ec}} = \left(\varepsilon_n^{\rho+} + m\hbar\Omega\right) + \varepsilon_n^{\rho-} + \varepsilon_n^{\sigma+} + \varepsilon_n^{\sigma-} = n\left(3 + 1/g\right)\Delta + m\hbar\Omega$ where n and m are integer numbers. The external electromagnetic field splits the conductivity peaks selectively. Because $V_{\mathbf{ec}}$ and Ω are bound by the condition (aceson), this imposes a constrain on the net photon-assisted tunneling (PAT) resonant current through the quantum well. We extract g and Δ from the d.c. PAT current-voltage characteristics. The splitting of the charged ρ_+ boson

peaks by the a.c. field helps to identifying of the Tomonaga Luttinger liquid state. The method is illustrated further in Fig. 9 where we show a single peak in $\mathcal{N}(\varepsilon)$ corresponding to a quantized free electron energy level [see Fig. 9(a)]. For non-interacting electrons ($g = 1$) the same single level splits either by an a.c. field due to the photon-assisted tunneling phenomena with spacing $\propto m\hbar\Omega$ (m being integer) or by a d.c. magnetic field with the Zeeman spacing $\propto \mu_B H$. The situation is remarkably different in the Luttinger liquid state when $g \neq 1$ and the charge ρ_+ and spin σ_+ levels have distinct energies $\varepsilon_n^{\rho+} \neq \varepsilon_n^{\sigma+}$. Then one easily identifies the charge and spin levels merely by applying the a.c. field and d.c. magnetic field to the same quantum well. If a level splits with spacing $\propto m\hbar\Omega$ by the a.c. field only (showing no response to the d.c. field) then it certainly is a ρ_+ charge boson level ($g \neq 1$). If it splits by the d.c. magnetic field [12] with the Zeeman spacing $\propto \mu_B H$ showing no response to the a.c. field, then it must be associated with the spin bosons σ_+. However if the both a.c. and d.c. magnetic fields split the same level, then the level belongs to the non-interactive electrons ($g = 1$) as had been said above. In this way one perceives the charge and spin bosons in experiments when applying a.c. electromagnetic field in combination with the d.c. magnetic field to a carbon tube junction. An important requirement to the experimental metallic carbon tube quantum well samples is that they must be clean.

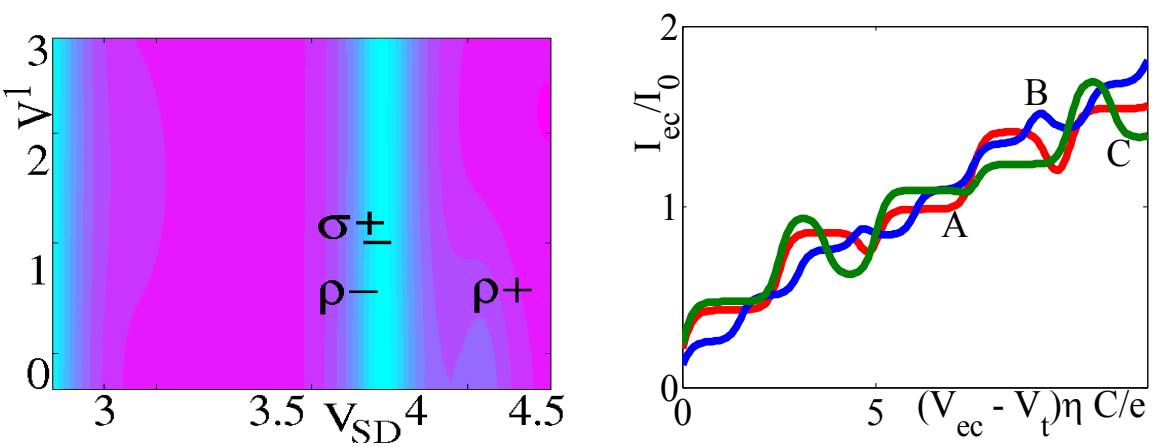

Fig. 10. (a) The contour plot σ (V_{ec},$V^{(1)}_{e,c}$) [V_{ec} and the a.c. bias amplitude $V_{e,c}^{(1)}$ being in units of Δ/e]. (b)The Coulomb staircase in the PASET current-voltage characteristics I(V_{dc}) versus reduced voltage V_{dc} (see text) of the CNT junction in the TLL state with g=0.4 under influence of the a.c. bias field with the amplitude $eV^{(1)}$=3.4 (in units of δ = e^2/C) and for a symmetric junction (η = 0.5). Curve A corresponds to Ω = 4.7, curve B to Ω = 3.7 and curve C to Ω = 6.7.

An electron-impurity scattering in real samples leads to a formation of additional pairs of combs with different periods. Then, an identification of the TLL state becomes possible with a mere generalization of the method described above. Ratio of the noise power to the mean current (Fano factor) is computed as $F = \sum_n T_n(1-T_n) / \sum_n T_n$ where the summation is performed over the conducting channels. Remarkably, the multiphoton absorption is pronounced in the noise spectra as well. In this way we suggest a method of the noise spectroscopy for studying of the photon-assisted tunneling into the TLL state.

Phenomena considered in this part of work originate from a specific physics of the charge and spin carriers, behaving like a blend of four non-interacting bosons. The Tomonaga Luttinger

liquid state occurs inside the one-dimensional quantum well formed by a metallic single wall carbon tube. The TLL state is tested with applying of an external a.c. electromagnetic field and of a d.c. magnetic field simultaneously. The a.c. field splits the charge boson energy levels due to the photon-assisted tunneling while the d.c. magnetic field splits the spin boson levels due to the Zeeman effect. That allows a mere identification of the quantized energy levels associated with the charge and spin bosons forming the TLL state in relevant experiments. Besides, one also determines the quantized level spacing Δ and the TLL parameter g. The unconventional electronic and photonic properties of the metallic carbon tube quantum well can be utilized in various nanodevice applications including THz field sensors and nanoemitters.

3. Directional photoelectric current across the bilayer graphene junction.

Electromagnetic properties of the bilayer graphene [31-34] offer enormous opportunities for scientific research and various nanoelectronic applications. They emerge in spectroscopy of bound and scattering states, in the photon-assisted chiral tunneling and in direct probing of strong correlation effects. Potential applications include electromagnetic field (EF) spectral analyzers, receivers, detectors, and sensors[B]. The crystal lattice of the bilayer graphene [31-34] consists of four equivalent sublattices of carbon atoms while the charge carriers behave there as massive "chiral fermions"[31,34]. The chiral fermions (CF) in bilayer graphene have a finite mass $m_{e,h}$, like conventional electrons (e) and holes (h) in metals and semiconductors [31-34]. The chirality relates the particles to certain sublattice and is responsible for various unconventional d.c. electronic and magnetic properties of the bilayer graphene [31]. In contrast to an ordinary tunneling through a conventional potential barrier, during the chiral tunneling (CT) an incoming electron is converted into a hole moving inside the graphene barrier in a reverse direction as indicated in Fig. 11a (Klein paradox[38,39]). This yields a finite transparency $T \neq 0$ for incident electrons with energies E below the barrier $E < U_0$ (U_0 is the barrier height energy) occurring [31] at finite particle incidence angles $\phi \neq 0$. On the other hand, the steady state chiral tunneling is blocked ($T = 0$) in the longitudinal direction $\phi = 0$. The angle-dependent transparency makes the chiral tunneling being attractive for various nanoelectronic applications [B]. The potential barrier in graphene can either be induced by the gate voltage $V_{\mathbf{G}}$ from a Si gate slab or can be formed by three overlapping graphene sheets as shown in Figs. 9(c,d). According to Ref. [31], the d.c. gate voltage $V_{\mathbf{G}}$ shifts the graphene barrier height, which controls the chiral tunneling. That process implies the wavefunction phases of electrons and holes being interconnected with each other in the graphene. The phase correlations during the chiral tunneling can also be directly tuned by applying of an external a.c. field. Controlling of the electron wavefunction phase by an a.c. field had not been accomplished yet and is the subject of this paper. The electronic properties are described by a spinor wavefunction $\hat{\Psi}$, which components depend on the angle ϕ between the electron momentum $\mathbf{p}$ and the x -axis (see Fig. 11). Similar spinor description had formerly been used for Dirac fermions [38] and for relativistic quasiparticles in single-layer graphene [31,32]. This part of work is devoted to electromagnetic properties of a bilayer graphene junction shown in Fig. 11. One may expect that the differential tunneling conductance $\sigma(\phi, V_{\mathbf{sd}})$ of "clean" samples depends on the angle ϕ between the electric current $\mathbf{j}$ and the x-direction (see Fig. 11). The whole shape of $\sigma(\phi)$ versus the source-drain voltage $V_{\mathbf{sd}}$ is very sensitive to properties of the bilayer graphene barrier. We begin with computing of the steady state $\sigma(\phi, V_{\mathbf{sd}})$ curves for a graphene barrier biased by $V_{\mathbf{sd}}$. The steady state results are then utilized for studying of the a.c. properties. When an external electromagnetic field (EF) is applied, it strongly affects the directional diagram of $\sigma(\phi, V_{\mathbf{sd}})$. In particular we will see that the external electromagnetic field

induces a finite conductance in the straightforward direction ($\phi = 0$), which had been blocked in the steady state.

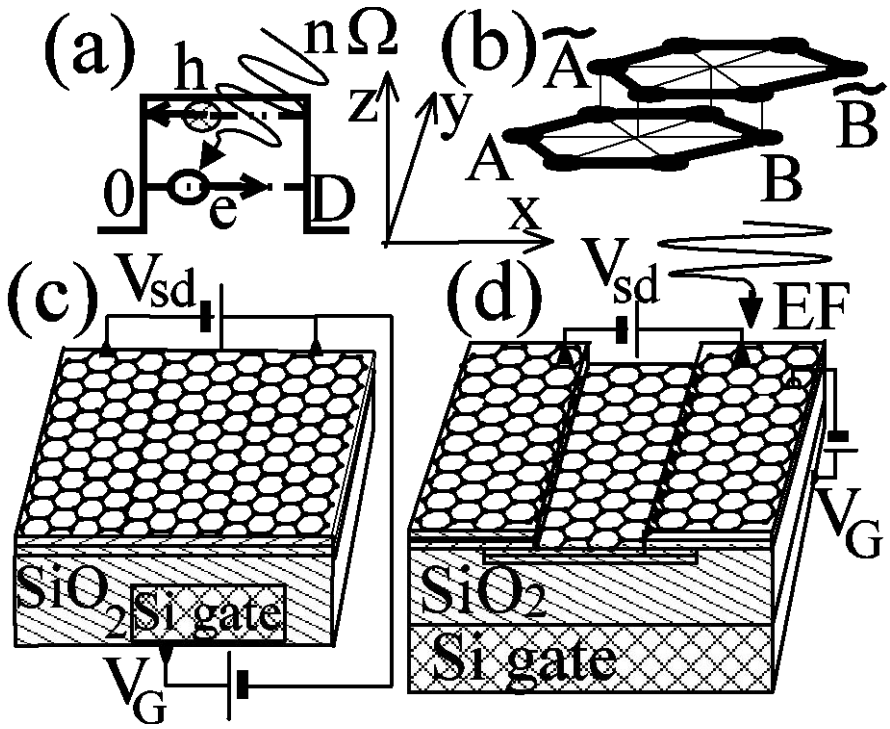

Fig. 11. (a) Potential barrier in the bilayer graphene controlled by the gate voltage V_G and exposed to the external electromagnetic field EF. The scattering states inside the barrier originate from conversion of an electron (e) to a hole (h). (b) Two coupled hexagonal lattices with non-equivalent carbon atomic sites A, B, $\tilde{A}$, and $\tilde{B}$ in the bottom and top layers respectively. (c) and (d) show two possible setups of the bilayer graphene junction. The external a.c. field induces the directional photon-assisted resonant tunnelling.

That happens because the electromagnetic field affects the electron-hole phase correlations inside the graphene barrier directly. In the steady state, when the a.c. field is off, the electric current is fully suppressed at $V_{\mathbf{sd}} < U_0$ (for typical gate voltage $V_{\mathbf{G}} = 1$ V and the SiO_2 thickness $d = 300$ nm one finds [32] $U_0 = 2$ meV).

Photon-assisted chiral tunneling

Here we examine influence of an electromagnetic field to chiral tunneling and discuss the intrinsic noise. For studying of the non-stationary electric current across the bilayer graphene junction we implement methods [21,22]. The graphene bilayer is modelled as two coupled gexagonal lattices consisting of four non-equivalent sites A, B and Ã, in the bottom and top layers respectively [see Fig. 11(a)]. For graphene junctions having finite dimensions, the motion of chiral fermions is quantized. The quantization imposes additional constrains on the directional tunneling diagram. Permitted values of the angle $\tilde{\phi}_n$ inside the graphene barrier are obtained from boundary conditions along the y -direction, so the y -component of the electron momentum $\mathbf{p} = (\hbar k, \hbar q)$ is quantized as $\tilde{q}_n = n\pi / W$ (where W is the barrier width), which gives $\tilde{\phi}_n = \arctan\left[n\pi / (k'_\varepsilon W)\right]$ where

$$k_\varepsilon' = \sqrt{2m/\hbar^2}\sqrt{\left|\varepsilon - U_0\right| - \left|\varepsilon\right|\left(1-\cos 2\phi\right)/2}\ .$$

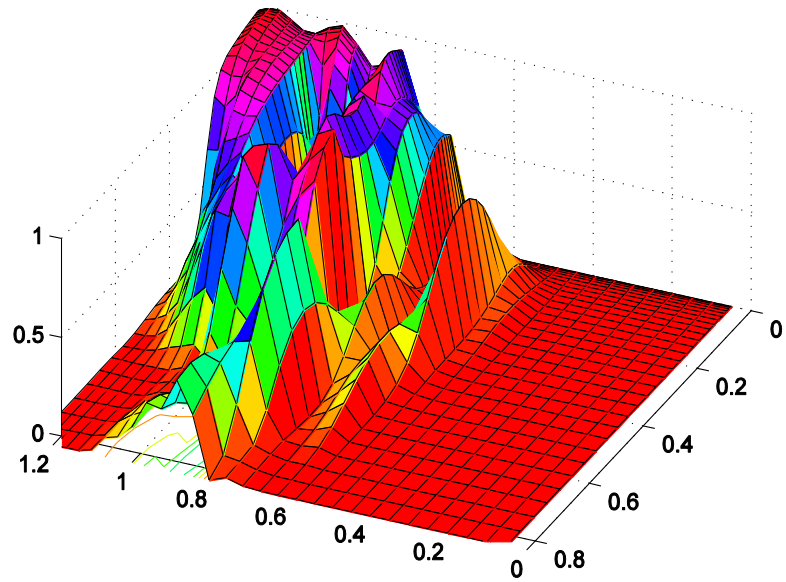

Fig. 12. A steady state differential conductivity $\sigma(\phi,V_{SD})$ [ϕ is the asimuthal angle, V_{SD} is the source drain bias voltage in units of the graphene barrier height eU_0] through the chiral barrier created by a bilayer graphehe pellet.

The external field not only splits the resonances, but also strongly affects angular dependence of the chiral tunneling. That happens because the a.c. field causes no influence to the $\hat{y}$ -component of the electron momentum q since the graphene barrier is effectively one-dimensional. The time dependence $\kappa_1\left(t\right)$ takes also place when the a.c. field modulates the graphene barrier width as $D \to D_0 + D_1 \cos\Omega t$. Splitting of the chiral tunneling resonances, and the angular redistribution of the electric current under the a.c. field influence is better pronounced for a finite barrier height $U_0 \neq 0$ and $U = U_0 + U_1 \cos\Omega t$. From Eq. (phi) one can see that $\phi' = 0$ if $\phi = 0$. However, if $\phi \neq 0$ one may observe spectacular phenomena. In this case an external a.c. field induces a finite electric current for an almost normal incidence $\phi \approx 0$, which was inhibited when the field was off. When $\phi \approx 0$, the a.c. field actually causes additional photon-assisted chiral tunneling resonances to engage. The directional photoelectric effect (DPE) may be realized in two scenarios. *One scenario* assumes that an electron beam having a finite angular width $\delta\phi \neq 0$ enters the graphene barrier normally. A visible DPE can be achieved in the setup shown in Fig. 13(b) where the attached electrodes 1,3 are made of one-dimensional conducting wires. If the wire is much narrower than the width of graphene stripe ($W_{\mathbf{w}} << W$), one may consider the electric current as a result of one-dimensional propagation of of electron along the trajectories under influence of the bias voltage. Such method formerly had intensively been used in numerous works devoted to point contact junctions. If the electric current is sufficiently weak, the electrons coming from the wire into the graphene stripe introduce a negligible disturbance into the electron spectrum inside graphene. The translational invariance inside graphene is well preserved. In an experiment one may use a STM tip for imaging of the electron wavefunction in carbon nanotube which show a periodic pattern. The electrode 1 emits electrons under a small but finite angle ϕ $(\phi << \pi,\ \ \phi \neq 0)$ which trajectories are focused/defocused by the external electromagnetic field as indicated in Fig.

13(b).

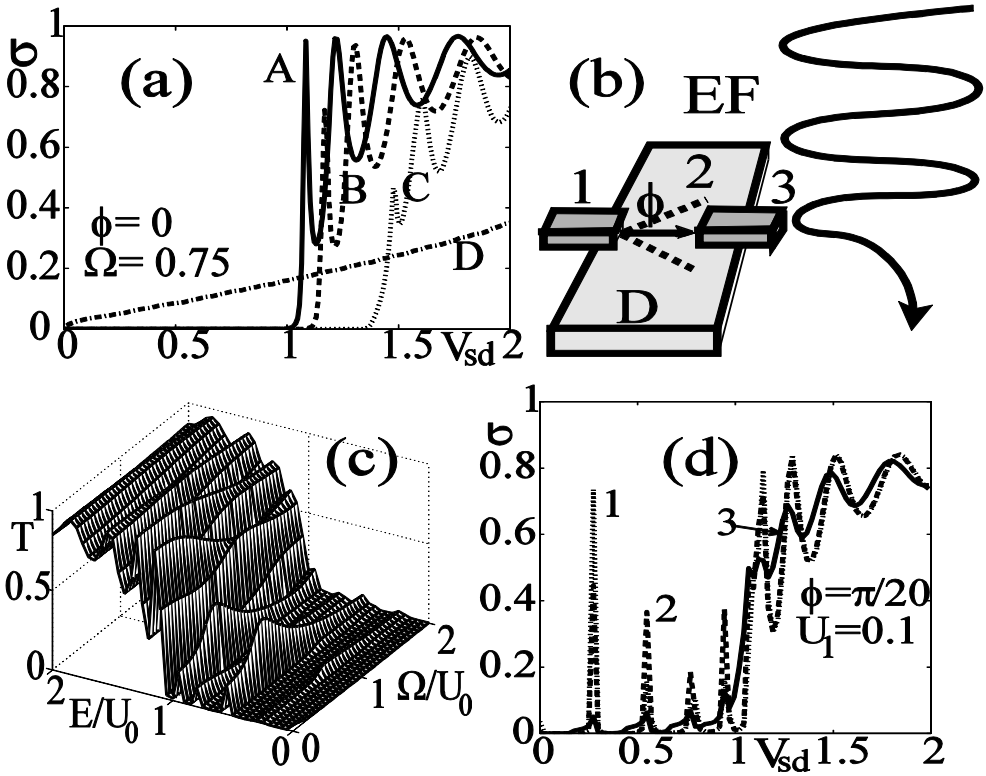

Fig. 13. The time averaged differential conductance $\bar{\sigma}^t(t)$[in units of $\sigma_0 = (2e^2/h)\pi(2mU_0)^{1/2}$] of a bilayer graphene junction exposed to an external electromagnetic field which modulates the barrier height $U(t) = U_0 + U_1 \cos\Omega t$. In Fig. 11(c) one may notice a remarkably strong DPE at $\Omega/U_0 \simeq 1$. This corresponds to curve 1 in Fig. 11(d) where the peak spacing is determined by the graphene barrier length D.

The frequency dependence of the transparency is governed by the directional photoelectric effect. A significant directional photo-electric effect emerges even for a relatively long wavelength $\lambda \simeq 1$ mm - 0.01 μm (which corresponds to the THz domain) if the condition $|E - U_0 \mp \Omega| << |E|$ is met. The deviation angle $\phi' = \arcsin[\sqrt{|E| / |E - U_0 \mp \Omega|}\sin\phi]$ inside the graphene barrier considerably increases giving $\phi' >> \phi$. This means that an ideal transparency taking place in the steady state at $\phi \neq 0$ is redistributed over the angle ϕ' after the a.c. field is applied. The transparency peaks are actually shifted from finite angles $\phi \neq 0$ to the normal incidence angle $\phi = 0$. *Another scenario* involves an incident single electron which enters the graphene barrier strictly in the normal direction ($\phi = 0$) under influence of a high frequency THz wave. In that scenario an electron absorbs a THz photon having the finite energy E_Ω and momentum q along the y-axis. Then the electron deviation angle $\delta\phi$ just before entering the barrier is small, $\delta\phi << \pi$. For instance taking $\nu = 30$ THz (which corresponds to the photon energy $E_\Omega = 125 \times 10^{-3}$ eV) one gets $\delta\phi \approx q / k = 2 \times 10^{-3}$. The photoelectric effect is well pronounced for an electron with energy $E_e \simeq 2 \cdot 10^{-3}$ **eV** after it gets inside the

graphene barrier. There if $\left|E-U_0\mp\Omega\right|<<\left|E\right|$ the deviation angle $\phi'=\arcsin[\sqrt{\left|E\right|/\left|E-U_0\mp\Omega\right|}\sin\phi]$ increases considerably, since the photon energy is pretty high, $E_\Omega\,/\,E_e\simeq 50, E_\Omega=0.1$ eV. Practically this means that one must set $\hbar\Omega\simeq U_0$ to get a strong photoelectric effect. In the above example the last condition also supposes that one should use $U_0\approx E_\Omega=125$ meV.

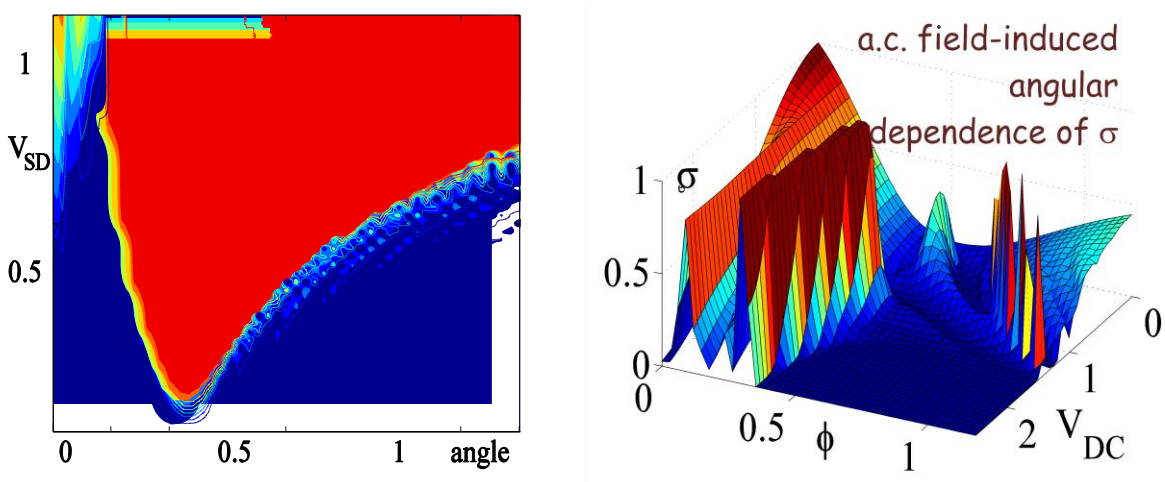

Fig. 14. (a) The contour plot σ(V_{SD},ϕ). (b) The 3d plot of σ(V_{SD},ϕ) where the additional angular dependence is induced by an external a.c. field applied.

Below we consider two most important field polarizations along the $\hat{x}$ and $\hat{z}$ axes as shown in Figs. 9(a,b). The barrier transparency $T(E,\phi)$ is affected by the a.c. field directly in either case. In particular, the barrier shape is modulated by the a.c. field polarized along the x -direction as sketched in Fig. 11(a), since $\epsilon\to\epsilon_0+\epsilon_1\cos\left(\Omega t\right)$. On other side, if one applies an a.c. field polarized as $\mathbf{E}=(0,0,E_z)$, it modulates the barrier height since $V_{\mathbf{G}}\to V_{\mathbf{G}}^{(0)}+V_{\mathbf{G}}^{(1)}\cos\left(\Omega t\right)$ [$V_{\mathbf{G}}^{(0)}$ is the steady state gate voltage, $V_{\mathbf{G}}^{(1)}$ is the a.c. field induced addition, see sketch in Fig. 11(b)]. Then the a.c. field induced correction to the d.c. tunneling current is $j_1=2e\int d\varepsilon\chi_\varepsilon\left|\delta t_{\varepsilon,\Omega}^{(1)}\right|^2\left(2n_\varepsilon-n_{\varepsilon+\Omega-eV}-n_{\varepsilon-\Omega-eV}\right)$, where the transmission amplitude $t_{\varepsilon,\Omega}^{(1)}$ is obtained from corresponding non-stationary boundary conditions at $x=0$ and $x=D$. Physically, the directional photoelectric effect (DPE) comes from an ingenuous influence of the external electromagnetic field to the electron-hole phase correlations during the chiral tunneling. Technically, modulation of the barrier height by the a.c. field shifts positions of the sharp peaks in the energy-dependent barrier transparency $T\left(\varepsilon\pm\Omega\right)$. Besides, it also modifies the overall angular distribution of the electric current, so the electron-hole conversions occur with an additional phase shift. Numerical results for both the cases are presented in Fig. 14(b). Corresponding plots for the steady state differential conductance $\sigma_0(V_{\mathbf{sd}})$ and for the photon-assisted chiral tunneling conductance $\sigma_1(V_{\mathbf{sd}})=\partial j_1\,/\,\partial V_{\mathbf{sd}}=\overset{-t}{\sigma}-\sigma_0$ both indicate the angular redistribution of the photon-assisted chiral tunneling current across the graphene barrier. The steady state conductance curve σ_0 in Fig. 14(b) corresponds to $U_0=2$ meV while curve σ_1 is computed for $V_{\mathbf{G}}=1$ V and $\Omega=1$ THz. The DPE is well illustrated by the sharp scattering resonance taking place in $\sigma_1(V_{\mathbf{sd}})$ [see the crisp peak at the incidence angle

$\phi = \pi / 16$ and at the bias voltage $V_{\mathbf{sd}} = U_0 = 0.5$ in Fig. 14(b)].

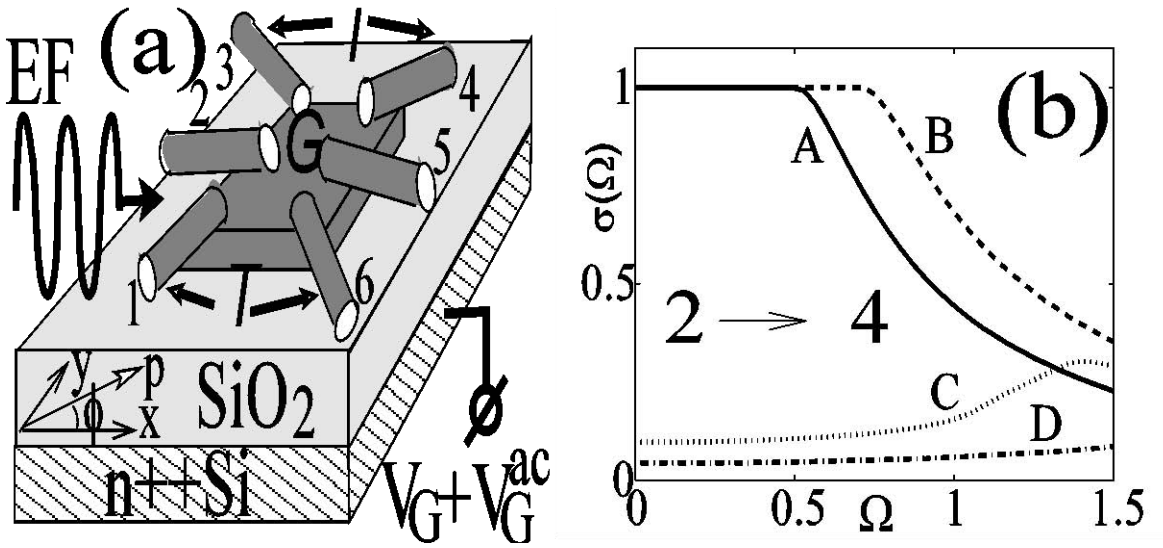

Fig. 15. (a) A setup consiststing of a graphene pellet G with ballistic transport of charge carriers. The angular distribution of the electric current is determined using carbon nanotube electrodes 1-6 attached to the pellet. The pellet and the nanotubes are laid on the SiO_2 substrate and are controlled by the gate voltage $V_G+V_G^{ac}$ where the 2nd term is induced by the external electromagnetic field EF. The EF also causes an angular redistribution of the time-averaged electric current which can be used for determining the THz field amplitude, frequency, and polarization. (b) The time-averaged differential conductivity between the carbon nanotube electrodes 2 and 4 versus the field frequency Ω [in units of $\hbar\Omega / e$] for different field amplitudes (curves A, B, C, and D).

When the a.c. field is off, the steady state tunneling at $V_0 = 0.5$ in the straightforward direction is suppressed [see the corresponding curve $\sigma_0\left(V_{\mathbf{sd}}\right)$ for $\phi = 0$]. However, if one applies the a.c. field with frequency Ω and $\mathbf{E} = (E_x, 0, 0)$, it opens tunneling channels in the straightforward direction $\phi = 0$ as is evident from curve σ_1 in Figs. 12(b). In Fig. 14(b) we compare two time-averaged conductance curves $\sigma_1\left(V_{\mathbf{sd}}\right)$ under influence of the a.c. field with two different polarizations along the $\hat{x}$ (curve X) and $\hat{z}$ (curve Z) axes correspondingly. In either case the $\sigma_1\left(V_{\mathbf{sd}}\right)$ curves show remarkable sharp peaks, which position however changes versus the field polarization. Although the above results are illustrative, they focus solely on the limit of a weak electromagnetic field $U_1 << U_0$.

Intrinsic noise in the bilayer graphene junction originates as follows. The thermal noise comes from the phonons emitted in the electron-phonon collisions. Matrix element of the electron-phonon collisions according to Ref. [43, 44] is $M_{pp'} \propto \left\langle p \middle| M(x) \middle| p' \right\rangle \cos\left(\phi_{pp'}\right)$ where $\phi_{pp'}$ is the angle between initial and final states. The phase factor $\cos\phi_{pp'}$ plays quite a different role in the bilayer graphene compared to the single layer graphene [43] where it is rather $\cos\left(\phi_{pp'} / 2\right)$ instead. In the latter case, the factor ensures suppression of the electron-phonon and electron-impurity collisions and the transport of the change carriers remains ballistic up to room temperatures. In contrast, thermal noise in the bilayer graphene devices is rather high at

room temperatures. Another intrinsic noise (Poisson noise) arises due to the "Zitterbewegung" effect, which is linked to a jittering motion of the change carriers when electrons are randomly converted to holes forth and back. That produces noise even in zero temperature limit. The noise is characterized by the Fano factor $F = \sum_n T_n \left(1 - T_n\right) / \sum_n T_n$, where T_n is the tunneling probability in the n-th channel and the summation is performed over all the conducting channels (in our setup this means just integration over the electron propagation angle ϕ). Our calculations show that the Poisson noise becomes extremally low at $V_{\mathbf{sd}} \geq U_0$.

In conclusion we computed the electric current across the bilayer graphene junction in conditions when an external electromagnetic field is applied. We have found that the threshold absorption of the external electromagnetic field strongly depends on the a.c. field frequency and amplitude. The electromagnetic field induces an ideal transparency of the graphene barrier in the longitudinal direction, which had been fully suppressed when the a.c. field was off. That directional photoelectric effect originates from an angular redistribution of the whole transparency diagram since the sidebands at finite angles are redirected to the normal incidence. An experimental observation of the spectacular directional optoelectric phenomena would provide a strong evidence for existence of the massive chiral fermions in the bilayer graphene. We emphasize that the threshold absorption emerges purely from a quantum mechanical phase shift, and not from an inelastic excitation by the a.c. field. That means no heating is involved during the absorption. The a.c. current induced by the electromagnetic field across the graphene junction has a sharp angular dependence, which potentially can be exploited in sensor nanodevices of the external electromagnetic field. The directional photoelectric effect in the double layer graphene junctions is a unique phenomenon which exists in that system and had not been noticed in other systems, like junctions composed of single layer graphene or of normal metals. Most intriguing feature is the switch between zero and finite conductance occurring without energy absorption. The phenomena considered above have a great potential for various nanoelectronic applications.

References

[1] M. S. Dresselhaus, G. Dresselhaus, and P. Avouris, Carbon tubes: synthesis, structure, properties, and applications, (Springer, New York, 2001).

[2] E. S. Snow, F. K. Perkins, E. J. Houser, S. C. Badescu, T. L. Reinecke, Science **307**,1942 (2005).

[3] S. Shafraniuk, EPL **87** 57007 (2009).

[4] V. P. Wallace, A. J. Fitzgerald, S. Shankar, R. J. Pye, D. D. Arnone, Brit. J. Derm. **151**, 424 (2004).

[5] J. Zhang, A. Boyd, A. Tselev, M. Paranjape, and P. Barbara, Applied Physics Letters **88**, 123112 (2006); A. Tselev, K. Hatton, M. S. Fuhrer, M. Paranjape, and P. Barbara, Nanotechnology **15**, 1475 (2004).

[6] J. Zhang, A. Tselev, Y. Yang, K. Hatton, P. Barbara and S. Shafraniuk, Phys. Rev. B **74**, 155414 (2006).

[7] D. Gunlycke, C. J. Lambert, S. W. D. Bailey, D. G. Pettifor, G. A. D. Briggs, and J. H. Jefferson, Europhys. Lett. **73**, 759 (2006).

[8] B. Babic and C. Schönenberger, Phys. Rev. B **70**, 195408 (2004).

[9] J. Cao, Q. Wang, H. Dai, Nature Materials **4**, 745 (2005).

[10] W. G. van der Wiel, S. De Franceschi, T. Fujisawa, J. M. Elzerman, S. Tarucha, and L. P. Kouwenhoven, Science **289**, 2105 (2000).

[11] J.W. Mintmire and C. T. White, Phys. Rev. Lett. **81**, 2506 (1998).

[12] C. L. Kane, L. Balents and M.P.A. Fisher, Phys. Rev. Lett. **79**, 5086 (1997).

[13] R. Egger and A. O. Gogolin, Phys. Rev. Lett. **79**, 5082 (1997).

[14] S. Tomonaga, Prog. Theor. Phys. **5**, 544 (1950); J.M. Luttinger, J. Math. Phys. (N.Y.) **4**, 1154 (1963).

[15] M. Bockrath et al., Nature (London) **397**, 598 (1999); Yao et al., Nature (London) **402**, 273 (1999).
[16] H. Ishii, H. Kataura, H. Shiozawa, H. Yoshioka, H. Otsubo, Y. Takayama, et al. Letters to Nature, **426**, 540 (2003).
[17] P. Recher, N. Y. Kim, and Y. Yamamoto, Phys. Rev. B **74**, 235438 (2006).
[18] Yu. V. Nazarov and L. I. Glazman, Phys. Rev. Lett. **91**, 126804 (2003).
[19] R. Tarkiainen, M. Ahlskog, J. Penttila, L. Roschier, P. Hakonen, M. Paalanen, and E. Sonin, Phys. Rev. B **64**, 195412 (2001).
[20] See V. Emery, in Highly Conducting One-Dimensional Solids, edited by J. Devreese et al. (Plenum, New York, 1979).
[21] L. V. Keldysh, Sov. Phys. JETP **20**, 1018 (1965).
[22] S. Datta, Electronic Transport in Mesoscopic Systems (Cambridge University Press, Cambridge, UK, 1997).
[23] D. V. Averin, A. N. Korotkov, and K. K. Likharev, Phys. Rev. B **44**, 6199 (1991).
[24] D. E. Feldman, S. Scheidl, and V. M. Vinokur, Phys. Rev. Lett. **94**, 186809 (2005).
[25] M. Trushin, A. L. Chudnovskiy, Europhys. Lett. **82**, 17008 (2008).
[26] V. F. Elesin and Yu. V. Kopaev, Sov. Phys. Uspekhi, **24**, 116 (1981).
[27] J. O ' Keeffe, C. Wei, and K. Cho, Appl. Phys. Lett., **80**, 676 (2002).
[28] C.-W. Chen, M.-H. Lee, and S. J. Clark, Nanotechnology, **15**, 1837 (2004).
[29] P. W. Chiu, M. Kaempgen, and S. Roth, Phys. Rev. Lett., **92**, 246802 (2004).
[30] Y. Li, S. V. Rotkin, and U. Ravaioli, Nanoletters, **3**, 183 (2003).
[31] Katsnelson M I, Novoselov K S and Geim A K 2006 Nature Phys. **2** 620
[32] Tworzydlo J, Trauzettel B, Titov M, Rycerz A, and Beenakker C W J 2006 Phys. Rev. Lett. **96** 246802
[33] Ando T 2005 J. Phys. Soc. Jpn. **74** 777.
[34] Nilsson J, Castro Neto A H, Guinea F, Peres N M R 2007 Phys. Rev. B**76** 165416.
[35] Fuse T, Kawano Y, Yamaguchi T, Aoyagi Y, and Ishibashi K 2007 Nanotechnology **18** 044001
[36] Kawano Y, Fuse T, Toyokawa S, Uchida S and Ishibashi K 2008 J. Appl. Phys. **103** 034307
[37] Kawano Y and Ishibashi K 2008 Nature Photon. **2** 618
[38] Strange P 1998 Relativistic Quantum Mechanics (Cambridge University Press, Cambridge, UK)
[39] Krekora P, Su Q and Grobe R, 2004 Phys. Rev. Lett. **92** 040406
[40] Novoselov K S, Geim A K, Morozov S V, Jiang D, Zhang Y, Dubonos S V, Grigorieva I V, Firsov A A 2004 Science **306** 666
[41] Yeyati A L and Buttiker M 1995 Phys. Rev. B **52** R14360
[42] Korn G A and Korn T M 1967 Handbook for Scientists and Engineers (New York: McGraw-Hill).
[43] Ando T, Nakanishi T and Saito R 1998 J. Phys. Soc. Jpn., **67** 2857; Ando T, Nakanishi T 1998 J. Phys. Soc. Jpn. **67** 1704
[44] McEuen P L, Bockrath M, Cobden D H, Yoon Y G, and Louie S 1999 Phys. Rev. Lett. **83** 5098

Personnel Supported

Dr. Serhii Shafraniuk Research Assistant Professor, Northwestern University, Evanston, IL

Publications

A. S. E. Shafraniuk, Nanosensors of External Fields, in Encyclopedia of Nanoscience and Nanotechnology, American Scientific Publishers (submitted in 2008).

B. S. Shafraniuk, Sensing an electromagnetic field with photon-assisted Fano resonance in two branch carbon nanotube junctions, Phys. Rev. B76, 085317 (2007).
C. S. E. Shafraniuk, Probing the intrinsic state of a one-dimensional quantum well with a photon-assisted tunneling, Phys. Rev. B 78, 235115 (2008).
D. S. E. Shafraniuk, Directional photoelectric effect in bilayer graphene quantum walls (nominated as the IOP Select), Journal of Phys.: Cond. Matt. 20, 015301 (2009).

Presentations

I. S. Shafraniuk, Department of Physics Colloquium, Georgetown University (2006).
II. "AC response of the carbon nanotube junction array to the external electromagnetic field", S. Shafraniuk, AFOSR Physics and Electronics Program Review Meeting, November 1-3, 2006, Arlington, VA. AFOSR Program Review, Quantum Electronic Solids, Carnegie Mellon University, Pittsburg, PA, August 7-9, 2006.
III. "Carbon nanotube sensors of THz electromagnetic fields", S. Shafraniuk, Colloquium @ Department of Electrical Engineering, State University of New York at Buffalo, April 13, 2007.
IV. "Electromagnetic properties of carbon nanotube and graphene quantum wells", Condensed Matter Seminar, Physics and Astronomy, Northwestern University (April 16, 2008).
V. "Nanotube sensor arrays of the THz electromagnetic field", S. Shafraniuk, AFOSR Nanoelectronics Program Review Meeting, Purdue University, May 22-23, 2007.
VI. "Multispectral Analyzing the THz field by a comb array of carbon tube junctions",Joint Electronics Program Review, Westin Arlington Gateway Hotel, Arlington, VA, 27-29 May 2009.
VII. "Zero-bias anomalies in multi-section carbon nanotube FETs" Yanfei Yang , Georgy Fedorov , Serhii Shafraniuk , Rupert Lewis , Benjamin Cooper , Christopher Lobb , Paola Barbara, 2009 APS March Meeting, March 16–20, 2009; Pittsburgh, Pennsylvania
VIII. "Zero-bias anomaly and possible superconductivity in single-walled carbon nanotubes", Zhang, Jian; Tselev, Alexander; Yang, Yanfei; Hatton, Kyle; Barbara, Paola; Shafraniuk, Serhii, APS March Meeting, March 5-9, 2007.